arXiv:1604.04551v4 [cond-mat.mtrl-sci] 10 Nov 2016

Single crystal growth from separated educts and its application to lithium transition-metal oxides

F. Freund[1], S. C. Williams[2], R. D. Johnson[2], R. Coldea[2], P. Gegenwart[1] and A. Jesche[1]

[1] *EP VI, Center for Electronic Correlations and Magnetism, Augsburg University, D-86159 Augsburg, Germany*

[2] *Clarendon Laboratory, University of Oxford, Parks Road, Oxford OX1 3PU, United Kingdom*

Thorough mixing of the starting materials is the first step of a crystal growth procedure. This holds true for almost any standard technique, whereas the intentional separation of educts is considered to be restricted to a very limited number of cases. A noticeable exception is the crystal growth in gels that allows for a better control of the nucleation by limiting the diffusion [1]. The successful application of this principle to open systems, however, has remained elusive. Here we show that single crystals of α-Li_2IrO_3 can be grown from separated educts in an open crucible in air. Elemental lithium and iridium are oxidized and transported over a distance of typically one centimeter in an isothermal process. Single crystals grow from an exposed condensation point placed in between the educts. The method has also been applied to the growth of Li_2RuO_3, Li_2PtO_3 and β-Li_2IrO_3 and a successful use for various other materials is anticipated.

The honeycomb iridates α-Li_2IrO_3 and Na_2IrO_3 attracted a lot of attention after Khaliullin and co-workers proposed that these systems offer a physical realization of the Kitaev interaction [2] in a solid [3,4]. Motivated by their proposal, several experimental studies on single crystalline Na_2IrO_3 and polycrystalline α-Li_2IrO_3 have been performed [5–7]. Direct evidence for the entanglement between spatial and spin directions, which is a consequence of the Kitaev exchange coupling, was recently observed in Na_2IrO_3 by means of diffuse magnetic X-ray scattering [8]. These experiments were facilitated by the availability of sizable single crystals [5], however, the microscopic details of the growth are not well understood. For α-Li_2IrO_3 it has not been possible so far to obtain single crystalline material − not even on a length scale of 10 µm. Accordingly, there has been no direct access to the anisotropy of the physical properties, and the magnetic structure as well as the contribution of the Kitaev exchange has been still under debate.

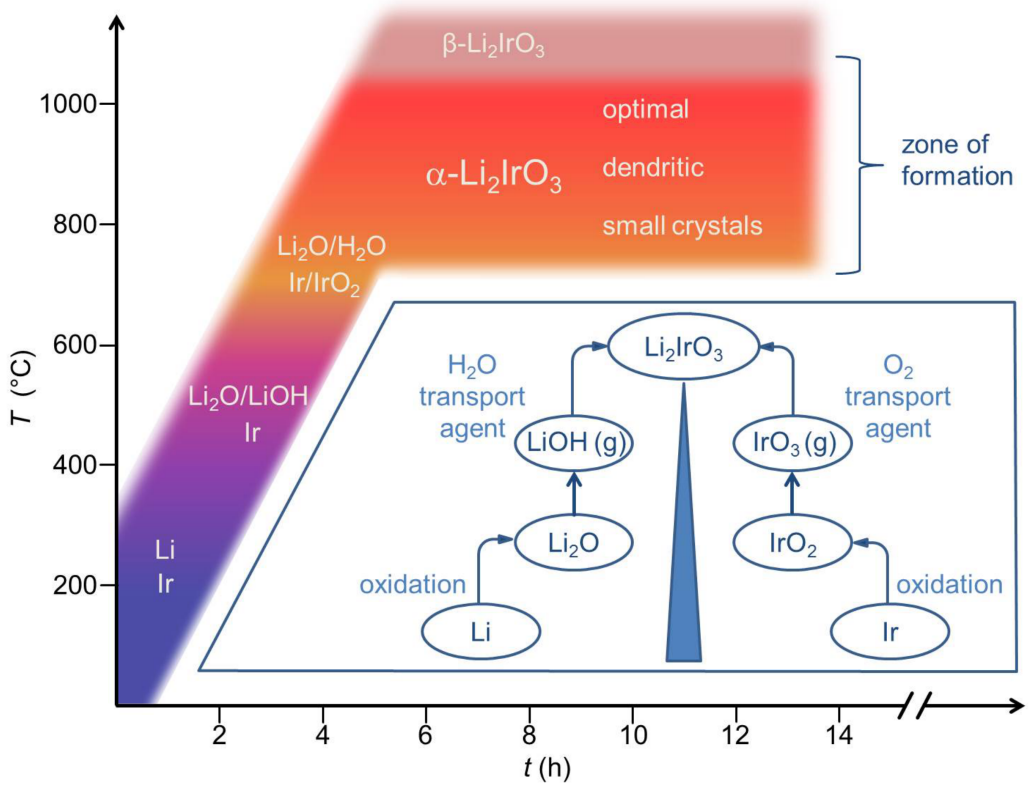

Figure 1: Schematic description of the synthesis method (inset) and temperature profile. Elemental Li and Ir are spatially separated in an open crucible. Upon heating in air Li initially forms solid LiOH that transforms to Li_2O at $T > 500\,°C$. Ir partially oxidizes to IrO_2. The formation of α-Li_2IrO_3 takes place at $T = 750\,°C - 1050\,°C$. Single crystals grow from an exposed condensation point placed in between the educts.

The growth procedure presented in this letter allows the growth of single crystals of α-Li_2IrO_3 of one millimeter along a side. A schematic sketch of the synthesis method and the phase formation as function of time and temperature are shown in Fig. 1. A remarkable feature is the isothermal nature of the process that was revealed by careful temperature measurements at different positions of the crucible (see Supplementary Figure 1): instead of a temperature gradient, here $< 1\frac{\mathrm{K}}{\mathrm{cm}}$, it is the formation of α-Li_2IrO_3 itself that drives the transport by maintaining a concentration gradient. The proposed, relevant transport equations are:

$$\mathrm{Li_2O(s) + H_2O(g) \rightleftharpoons 2\,LiOH(g)} \qquad \text{[9, p. 166]}$$

$$\mathrm{IrO_2(s) + \frac{1}{2}O_2(g) \rightleftharpoons IrO_3(g)} \qquad \text{[9, p. 217]}$$

Single crystalline α-Li_2IrO_3 forms from gaseous LiOH and IrO_3. The X-ray diffraction pattern and the sharpness of the phase transition to the magnetically ordered state revealed a superior sample quality when compared to polycrystalline material (see below). Furthermore, the magnetic structure has been solved by recent single crystal magnetic resonant X-ray diffraction measurements performed on these samples (published separately [10]). The synthesis of α-Li_2IrO_3 was first reported by Kobayashi *et al.* in 1997 [11]. Polycrystalline material was obtained by heating mixtures of Li_2CO_3 and IrO_2 to temperatures between 650 °C − 1050 °C. The presence of a low-spin Ir^{4+} state with an effective spin 1/2, as one of the essential ingredients of the Kitaev model, was reported soon after [12]. Despite the substantial interest in this material, the basic synthesis root has not changed since: to the best of our knowledge all attempts made are based on using Li_2CO_3 as starting material. Heating mixtures of Li_2CO_3 with Ir or IrO_2 to sufficiently high temperatures leads to the formation of α-Li_2IrO_3 under release of CO_2. This process, often referred to as 'calcination', has been applied to the growth of several other related materials, e.g.: Li_2RuO_3 [13], Na_2IrO_3 [14] or Na_2PtO_3 [14]. In this way comparatively large single crystals of Na_2IrO_3 were obtained [5, 8]. The samples show a plate-like habit with typical lateral dimensions of a few square millimeter and a thickness of 100 μm. They grow out of a polycrystalline base ('poly bed') and form predominantly at the upper part of the product. For α-Li_2IrO_3, however, the similar approach leads to only a fine powder. Different flux methods, especially pre-sintered α-Li_2IrO_3 in LiCl flux, failed to increase the crystal size. Nevertheless, a better crystallinity was inferred from X-ray powder diffraction measurements [15]. In those attempts, the LiCl does not act as a 'classical' flux, it rather promotes a solid state reaction with enhanced diffusion.

At temperatures above 1000 °C the formation of α-Li_2IrO_3 competes with the high-temperature polytype β-Li_2IrO_3 [16]. After repetitive heating of α-Li_2IrO_3 at 1100 °C small single crystals up to several 10 µm of β-Li_2IrO_3 form [17]. Annealing β-Li_2IrO_3 at temperatures below 1000 °C did not lead to the formation of α-Li_2IrO_3, indicating that the transition is irreversible. Small single crystals of a third modification, the 'harmonic' honeycomb γ-Li_2IrO_3, were obtained by the calcination of Li_2CO_3 and IrO_2 followed by annealing in molten LiOH at 700 °C to 800 °C [18]. An advantage of the calcination process is the ability to start from carbonates which are comparatively easy to handle and store. In contrast, elemental lithium is air sensitive and has been avoided as an educt in previous approaches. Furthermore, lithium reacts with many standard crucible materials and develops a moderately high vapor pressure (17 mbar at 900 °C [19]). On the other hand, elemental lithium

has several advantages for the use as a flux. Its low melting point of 180 °C in comparison with a high boiling temperature of 1342 °C fulfill two key characteristics of a good flux [20]. Furthermore, lithium has a good solubility for iridium [21]. However, all our attempts to grow single crystals of α-Li_2IrO_3 from a lithium-rich flux and mixtures of lithium with LiCl, LiOH, $LiBO_2$ and/or Li_2CO_3 failed. A comprehensive overview of those attempts is given in the Supplementary Table 1.

Comparatively large single crystals of several millimeter along a side, as observed for Na_2IrO_3 [5, 8] are not expected to grow in a solid state reaction due to the limited diffusion length. Given that the calcination process is completed at these temperatures (at 1050 °C) and the compound does not melt congruently indicates the relevance of a vapor transport process within the crucible. In order to investigate the possible formation and transport of Li-O, Ir-O, and/or Li-Ir-O gas specious during the syntheses of α-Li_2IrO_3, we started a growth attempt from elemental lithium and iridium in air. Lithium granules were placed on iridium powder in an Al_2O_3 crucible. The mixture was heated to 900 °C over 4 h, held for 72 h and quenched to room temperature. To our surprise, already the first attempt revealed α-Li_2IrO_3 single crystals of up to 50 µm along a side. The whole product appeared homogeneous and X-ray powder diffraction pattern showed only small amounts of IrO_2 and Ir. This is even more surprising since only three small lithium granules (roughly 4 mm in length with a diameter of 1.5 mm) were used but α-Li_2IrO_3 formed over the whole bottom of the crucible (inner diameter of 16 mm). This observation strongly supports the idea of vapor transport playing a decisive role for the growth of this material. However, a classical vapor transport along a temperature gradient does not seem to take place: various growth attempts in a horizontal tube furnace indicated that once α-Li_2IrO_3 has formed it does not transport anymore. This observation is corroborated by an estimate of the free enthalpy of formation for α-Li_2IrO_3: $\Delta H^0_{\mathrm{B},\,298} = -880 \frac{\mathrm{kJ}}{\mathrm{mol}}$ and $S^0_{298} = 89 \frac{\mathrm{J}}{\mathrm{mol \cdot K}}$ [M. Schmidt, MPI-CPfS, private communication]. It corresponds to a large, exothermic value of the free reaction enthalpy of $-332 \frac{\mathrm{kJ}}{\mathrm{mol}}$ for the following equilibrium equation:

$$\mathrm{IrO_3(g)} + 2\ \mathrm{LiOH(g)} \longrightarrow \mathrm{Li_2IrO_3(s)} + \mathrm{H_2O(g)} + \frac{1}{2}\mathrm{O_2}$$

Therefore, we started to investigate the growth from spatially separated educts. For this purpose a specially designed setup has been constructed as depicted in Fig. 2a−c. It consists of a standard crucible, rings (washers), rings with spikes and a disc with a center hole (aperture). All parts are made from Al_2O_3. The rings act as spacers, hold the aperture in place and allow to vary the distance between starting materials and spikes.

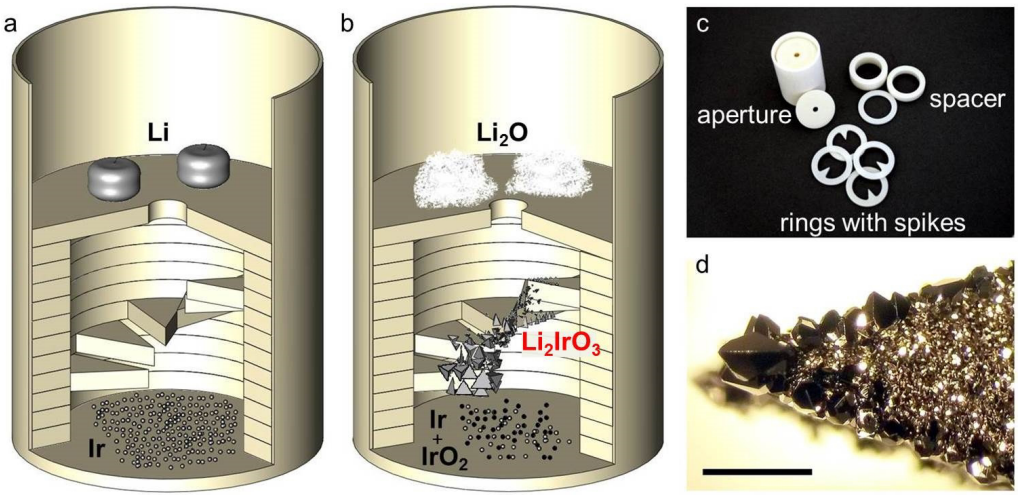

Figure 2: Crystal growth equipment (crucible diameter 16 mm). Arrangement of the materials before and after the growth process is depicted in a) and b), respectively. The rings with spikes are oriented like a spiral staircase in order to allow for nucleation at different positions with less intergrowth of the crystals. Formation of the largest α-Li_2IrO_3 single crystals is observed on spikes placed roughly 4 mm above the Ir starting material. c) individual setup parts made from Al_2O_3 and d) typical appearance of one of the lower spikes covered with α-Li_2IrO_3 crystals at the bottom side, scale bar 1 mm.

The spikes provide an exposed condensation point in between the educts. They are stacked as a 'spiral staircase' in order to identify the ideal position for the growth. The aperture is placed above the spikes and acts as a platform for one of the starting materials. The other educt is placed on the bottom of the crucible in the center of two spacers. This avoids a direct contact between the material and the spikes which sit on top of the spacers. For the growth of α-Li_2IrO_3, iridium metal powder and lithium granules are used as starting materials. Iridium is placed on the bottom of the crucible, lithium on top of the aperture. The distance between the elements is roughly 11 mm with five spikes placed in-between. The masses were chosen in their stoichiometric ratio. The whole setup is placed in a box furnace at 200 °C, heated to 1020 °C with a rate of 180 °C per hour, held for three days and finally quenched to room temperature. While heating, lithium transforms to a Li_2O/LiOH mixture at moderate temperatures. At 900 °C all lithium is burned to Li_2O. See a detailed analysis of this process in the Supplementary Figure 2. Only small amounts of Li_2O are found on top of the aperture (where the lithium was placed) after the process. The iridium powder placed at the bottom is partially oxidized to IrO_2. α-Li_2IrO_3 covers large parts of the spikes, with the largest crystals growing at the tip of the spikes, $3-4$ mm above the iridium (Fig. 2d).

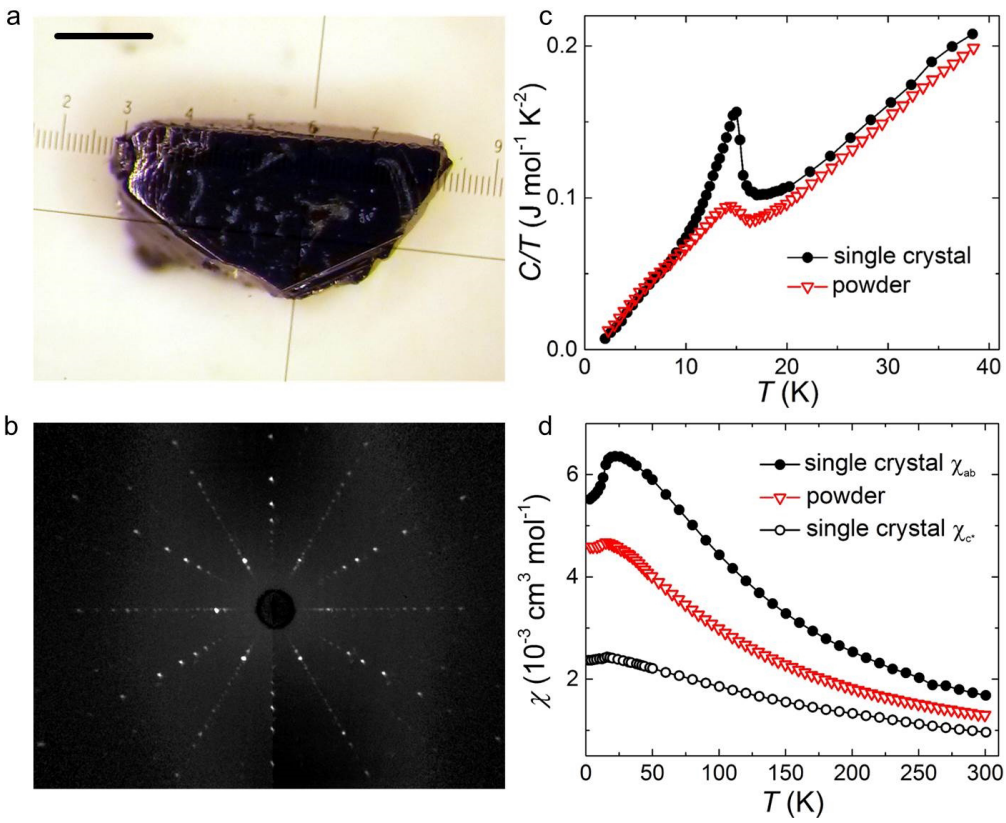

Figure 3: Sample quality and magnetic anisotropy of α-Li_2IrO_3. a) comparatively large single crystal (1.2 mm × 0.4 mm × 0.5 mm and $m = 1.7$ mg) grown from separated educts (scale bar 0.3 mm). The corresponding Laue-back-reflection pattern, depicted in b), shows the (nearly) three-fold rotation symmetry perpendicular to the honeycomb layers. c) temperature dependent specific heat of the single crystal shown in a) in comparison with a typical polycrystalline sample. d) an easy-plane anisotropy is apparent from the temperature dependent magnetic susceptibility ($\mu_0 H = 1$ T, $\chi_{ab} : H \perp c^*$, $\chi_{c^*} : H \parallel c^*$).

Single crystals of dimensions larger than 1 mm were obtained (Fig. 3a). A good sample quality is inferred from Laue-back-reflection (Fig. 3b): the diffraction pattern shows the (nearly) three-fold rotational symmetry of the honeycomb layers (along the $\boldsymbol{c}^*$-direction). The spot-size of the X-ray beam was similar to the sample dimensions. Figure 3c shows the temperature dependent specific heat measured on the same single crystal in comparison with polycrystalline material that was grown by calcination [6]. The improved sample quality of the single crystal is apparent from a sharper transition to the antiferromagnetically ordered state at $T_N = 15$ K. Temperature-dependent magnetic susceptibility for field applied parallel (χ_{ab}) and perpendicular (χ_{c^*}) to the honeycomb layers is shown in Fig. 3d. An easy-plane behavior with a sharp decrease of χ_{ab} at T_N is observed, whereas χ_{c^*} de-

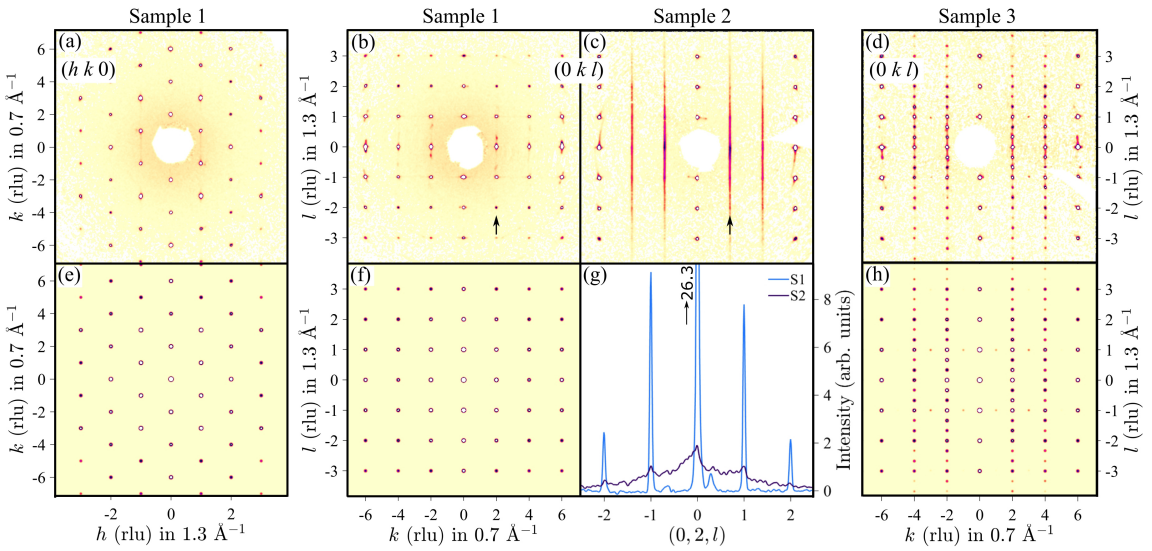

Figure 4: X-ray diffraction pattern from three different α-Li_2IrO_3 crystals: one un-twinned and without stacking faults (sample 1, panels a−b), one predominantly a single grain, but with significant stacking faults manifested in extended diffuse scattering along l (sample 2, panel c), and one multi-twin crystal (sample 3, panel d). Color is intensity on a log scale. Vertical arrows near $k = 2$ in panels b−c show direction along which the intensity is plotted in panel g, note the strong contrast between sample 1 with sharp peaks at integer l and sample 2 where diffuse scattering dominates. Bottom graphs e, f, h show the calculated X-ray diffraction pattern in the same axes as the above panels a, b, d, for the nominal monoclinic crystal structure of α-Li_2IrO_3 [22]. Panel h includes contribution from $C^{\pm}$ twins (grains rotated by $\pm 120°$ around $\boldsymbol{c}^*$ leading to the peaks at fractional coordinates $(0, k, n \pm 1/3)$, with n integer and $k = \pm 2, \pm 4$) and an A-type twin responsible for the peaks at $(0, k, \pm 1)$ with k odd (see Supplementary Note for details).

creases only slightly. A measurement performed on polycrystalline material [6] is included for comparison and can be roughly described by $1/3\,\chi_{c^*} + 2/3\,\chi_{ab}$ for $T > T_N$.

The structural order in the grown crystals was probed using X-ray diffraction and representative patterns are shown in Fig. 4a−d. The data are fully consistent with the expected monoclinic crystal structure [22] of alternate stacking of honeycomb $Li_{1/2}IrO_3$ and hexagonal Li layers with space group $C2/m$ (calculated patterns shown in Fig. 4e−f). The unit cell parameters obtained from indexing the diffraction data are $a = 5.169(7)$Å, $b = 8.938(8)$Å, $c = 5.121(7)$Å, $\beta = 109.75(6)°$, consistent with the earlier powder data [22]. Samples grown at 900 °C showed pronounced rods of diffuse scattering along the $\boldsymbol{c}^*$ direction, normal to the layers, as evidenced in Fig. 4c. Rods of diffuse scattering with the same selection rule were also observed in the iso-structural materials Na_2IrO_3 and α-$RuCl_3$ [23] and attributed [24] to occasional in-plane shifts of the stacked layers by $\pm\boldsymbol{b}/3$. Monitoring the structural

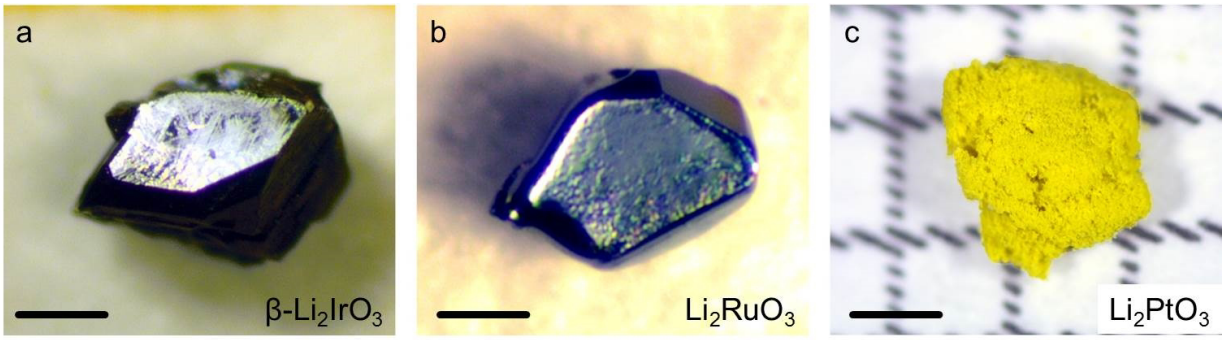

Figure 5: Further materials synthesized from separated educts. a) β-Li_2IrO_3 single crystal (scale bar 0.2 mm) and b) a single crystal of Li_2RuO_3 (scale bar 0.1 mm). For Li_2PtO_3 fine yellow powder could be obtained shown in c) (scale bar 1 mm).

order for different growth temperatures allowed us to optimize the synthesis parameters and obtain crystals with almost no detectable diffuse scattering (compare Fig. 4b−c, and the intensity profile in Fig. 4g), showing that those crystals grown at 1020 °C are close to the limit of fully-coherent, three-dimensional structural ordering. Fig. 4a−b show data from an un-twinned single crystal. Most as-grown crystals are twinned and a representative diffraction pattern shown in Fig. 4d can be understood by three additional twins: two twins rotated by ±120° around $\boldsymbol{c}^*$, and another twin with the $\boldsymbol{a}$ and $\boldsymbol{c}$ axes interchanged (for more details see Supplementary Note). We note that the susceptibility data in Fig. 3d was collected on a crystal that contained predominantly twins rotated by ±120° around $\boldsymbol{c}^*$, so under the assumption that the susceptibility tensor has only one unique axis $\boldsymbol{c}^*$ (normal to the *ab* plane), all those twins had the same magnetic response in field applied along $\boldsymbol{c}^*$ or perpendicular.

The method described is not restricted to the growth of α-Li_2IrO_3. Single crystals of β-Li_2IrO_3 and Li_2RuO_3 were also obtained (Fig. 5a, b, see Supplementary Figure 3 for X-ray diffraction pattern). Formation of the latter is expected from the similar transport behavior of Ir and Ru [9, p. 214 ff]. For Li_2PtO_3 we obtained polycrystalline material of good quality (Fig. 5c, see Supplementary Figure 3 for X-ray diffraction pattern). In conclusion, the technique should be applicable to various transport active elements in air in its simplest form. Application to a broader class of materials could be achieved by providing a controlled atmosphere (static or flowing) of, for example, oxygen, chlorine or iodine. The combination of an isothermal vapor transport in an open crucible with separated educts is unique and provides another approach for the crystal growth community.

The authors thank M. Schmidt, V. Tsurkan, A. Tsirlin, S. Manni, G. Hammerl, A. Erb, H. S. Jeevan, C. Krellner, S. Wurmehl, C. Geibel, T. Wolf, D. Schmitz and W. Scherer for fruitful discussions. For the technical support we like to thank A. Mohs, A. Herrnberger and K. Wiedenmann. This work has been supported by the German Science Foundation through projects TRR-80, SPP1666 and the Emmy Noether program - JE 748/1. Work in Oxford was partially supported by the EPSRC (UK) under Grants No. EP/H014934/1 and EP/M020517/1. R.D.J. acknowledges support from a Royal Society University Research Fellowship. In accordance with the EPSRC policy framework on research data, access to the data generated using EPSRC funds will be made available from X-ray data depository at http://dx.doi.org/10.5287/bodleian:O5YMYxv8R.

email: anton.jesche@physik.uni-augsburg.de

References

[1] Henisch, H. K., Dennis, J. & Hanoka, J. I. Crystal growth in gels. *J. Phys. Chem. Solids* **26**, 493–500 (1964).

[2] Kitaev, A. Anyons in an exactly solved model and beyond. *Ann. Phys.* **321**, 2–111 (2006).

[3] Jackeli, G. & Khaliullin, G. Mott insulators in the strong spin-orbit coupling limit: from Heisenberg to a quantum compass and Kitaev models. *Phys. Rev. Lett.* **102**, 017205 (2009).

[4] Chaloupka, J., Jackeli, G. & Khaliullin, G. Kitaev-Heisenberg model on a honeycomb lattice: possible exotic phases in iridium oxides A_2IrO_3. *Phys. Rev. Lett.* **105**, 027204 (2010).

[5] Singh, Y. & Gegenwart, P. Antiferromagnetic Mott insulating state in single crystals of the honeycomb lattice material Na_2IrO_3. *Phys. Rev. B* **82**, 064412 (2010).

[6] Singh, Y. *et al.* Relevance of the Heisenberg-Kitaev model for the honeycomb lattice iridates A_2IrO_3. *Phys. Rev. Lett.* **108**, 127203 (2012).

[7] Ye, F. *et al.* Direct evidence of a zigzag spin-chain structure in the honeycomb lattice: a neutron and x-ray diffraction investigation of single-crystal Na_2IrO_3. *Phys. Rev. B* **85**, 180403 (2012).

[8] Chun, S. H. *et al.* Direct evidence for dominant bond-directional interactions in a honeycomb lattice iridate Na_2IrO_3. *Nat. Phys.* **11**, 462–466 (2015).

[9] Binnewies, M., Glaum, R., Schmidt, M. & Schmidt, P. *Chemical Vapor Transport Reactions* (de Gruyter, Berlin/Boston, 2012).

[10] Williams, S. C. *et al.* Incommensurate counterrotating magnetic order stabilized by Kitaev interactions in the layered honeycomb α-Li_2IrO_3. *Phys. Rev. B* **93**, 195158 (2016).

[11] Kobayashi, H. *et al.* Structure and charge/discharge characteristics of new layered oxides: $Li_{1.8}Ru_{0.6}Fe_{0.6O3}$ and Li_2IrO_3. *J. Power Sources* **68**, 686–691 (1997).

[12] Kobayashi, H., Tabuchi, M., Shikano, M., Kageyama, H. & Kanno, R. Structure, and magnetic and electrochemical properties of layered oxides, Li_2IrO_3. *J. Mater. Chem.* **13**, 957–962 (2003).

[13] Dulac, J. F. Synthesis and crystallographic structure of a new ternary compound Li_2RuO_3. *C. R. l'Acad. Sci., Ser. B* **270**, 223–226 (1970).

[14] McDaniel, C. L. Phase relations in the systems Na_2O-IrO_2 and Na_2O-PtO_2 in air. *J. Solid State Chem.* **9**, 139–146 (1974).

[15] Manni, S. *Synthesis and investigation of frustrated Honeycomb lattice iridates and rhodates.* Ph.D. thesis, Georg-August-Universität Göttingen (2014).

[16] Takayama, T. *et al.* Hyperhoneycomb iridate β-Li_2IrO_3 as a platform for Kitaev magnetism. *Phys. Rev. Lett.* **114**, 077202 (2015).

[17] Biffin, A. *et al.* Unconventional magnetic order on the hyperhoneycomb Kitaev lattice in β-Li_2IrO_3: full solution via magnetic resonant x-ray diffraction. *Phys. Rev. B* **90**, 205116 (2014).

[18] Modic, K. A. *et al.* Realization of a three-dimensional spin–anisotropic harmonic honeycomb iridate. *Nat. Commun.* **5** (2014).

[19] Honig, R. E. & Kramer, D. A. Vapor pressure data for solid and liquid elements. *RCA Rev.* **30**, 285 (1969).

[20] Jesche, A. & Canfield, P. C. Single crystal growth from light, volatile and reactive materials using lithium and calcium flux. *Phil. Mag.* **94**, 2372–2402 (2014).

[21] Massalski, T. B., Okamoto, H. & Subramanian, P. R. *Binary Alloy Phase Diagrams, 2nd Edition (Volume 3)* (A. S. M. International, Materials Park, OH, 1990).

[22] O'Malley, M. J., Verweij, H. & Woodward, P. M. Structure and properties of ordered Li_2IrO_3 and Li_2PtO_3. *J. Solid State Chem.* **181**, 1803–1809 (2008).

[23] Johnson, R. D. *et al.* Monoclinic crystal structure of α-$RuCl_3$ and the zigzag antiferromagnetic ground state. *Phys. Rev. B* **92**, 235119 (2015).

[24] Choi, S. K. *et al.* Spin waves and revised crystal structure of honeycomb iridate Na_2IrO_3. *Phys. Rev. Lett.* **108**, 127204 (2012).

Supplementary Information to "Single crystal growth from separated educts and its application to lithium transition-metal oxides"

Supplementary Table 1: Results of various attempts to grow α-Li_2IrO_3 single crystals from flux.

Flux	Starting Material	Crucible	Temperature Profile	Result
Li	α-Li_2IrO_3	Ta	4 h to 1000 °C	crucible decomposed
Li	α-Li_2IrO_3	Nb	4 h to 1000 °C	crucible decomposed
Li	IrO_2	Nb	5 h to 1000 °C; hold 5 h; 60 h to 200 °C	Ir single crystals, crucible attacked
Li, $LiBO_2$	α-Li_2IrO_3	Pt in quartz	5 h to 950 °C; hold 1 h; 60 h to 500 °C	quartz tube broken, α-Li_2IrO_3 transformed to IrO_2
LiCl, Li_2CO_3	α-Li_2IrO_3	Al_2O_3 in quartz	2 h to 1000 °C; hold 2 h; 55 h to 500 °C	well ordered α-Li_2IrO_3 powder, β-Li_2IrO_3 impurities
LiCl, LiOH	α-Li_2IrO_3	Al_2O_3 in quartz	2 h to 1000 °C; hold 2 h; 55 h to 500 °C	well ordered α-Li_2IrO_3, β-Li_2IrO_3 and IrO_2
LiCl, Li_2CO_3	α-Li_2IrO_3	Al_2O_3 in quartz	2 h to 850 °C; hold 2 h; 55 h to 500 °C	α-Li_2IrO_3 pellet not solved in flux
LiCl, LiOH	α-Li_2IrO_3	Al_2O_3 in quartz	2 h to 850 °C; hold 2 h; 55 h to 500 °C	α-Li_2IrO_3 powder
LiOH	α-Li_2IrO_3	Al_2O_3 in Nb	8 h to 800 °C; hold 6 h; 50 h to 500 °C	α-Li_2IrO_3 powder, Ir impurities
LiCl	α-Li_2IrO_3	Al_2O_3 in quartz	2 h to 850 °C; hold 2 h; 55 h to 500 °C	α-Li_2IrO_3 powder, β-Li_2IrO_3 and IrO_2 impurities

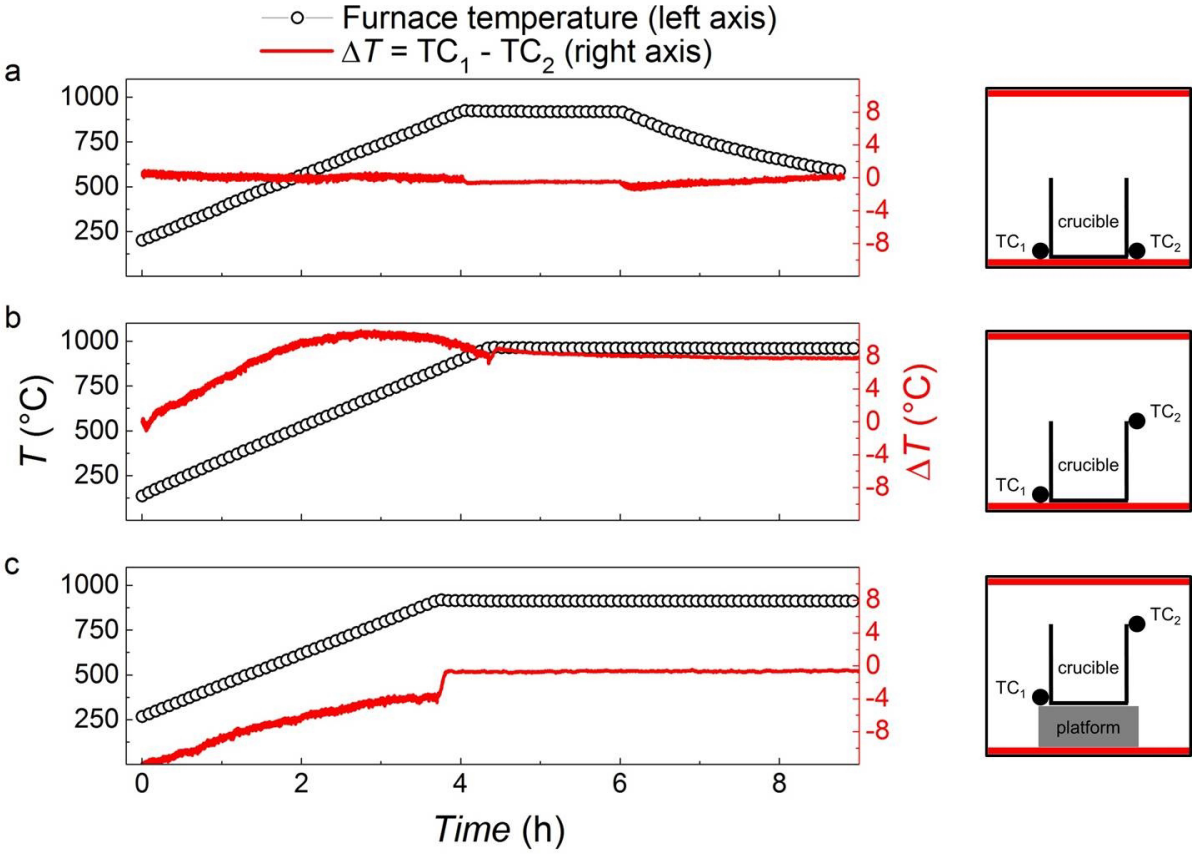

Supplementary Figure 1: Temperature gradient between bottom and top of the crucible during the growth. Temperature profiles are shown on the left hand side. The position of the thermocouples (TCs) are depicted on the right. The heating plates of the furnace are placed on the top and bottom (marked in red). a), verification of the calibration of the used thermocouples. TC_1 and TC_2 are both placed on the bottom of the crucible. The crucible stands on the lower heating plate. A small difference in the range of $\Delta T \approx \pm 1\,°C$ is confirmed. b), TC_1 stays at the bottom and TC_2 is placed on the top. The gradient increases during the heating process. At the final temperature the difference is constant and small with $\frac{\Delta T}{\Delta z} \approx \frac{8\,K}{2\,cm} = 4\frac{K}{cm}$. c), in order to investigate the effect of the small temperature gradient observed in b), the whole setup is placed on a platform to equalize the distance of the crucible to the upper and lower heating plate of the furnace. As expected for a symmetric arrangement $\Delta T \approx 0\,K$. The growth is not affected and it is still possible to grow α-Li_2IrO_3 single crystals in this configuration. This shows the minor importance of a temperature gradient in this method.

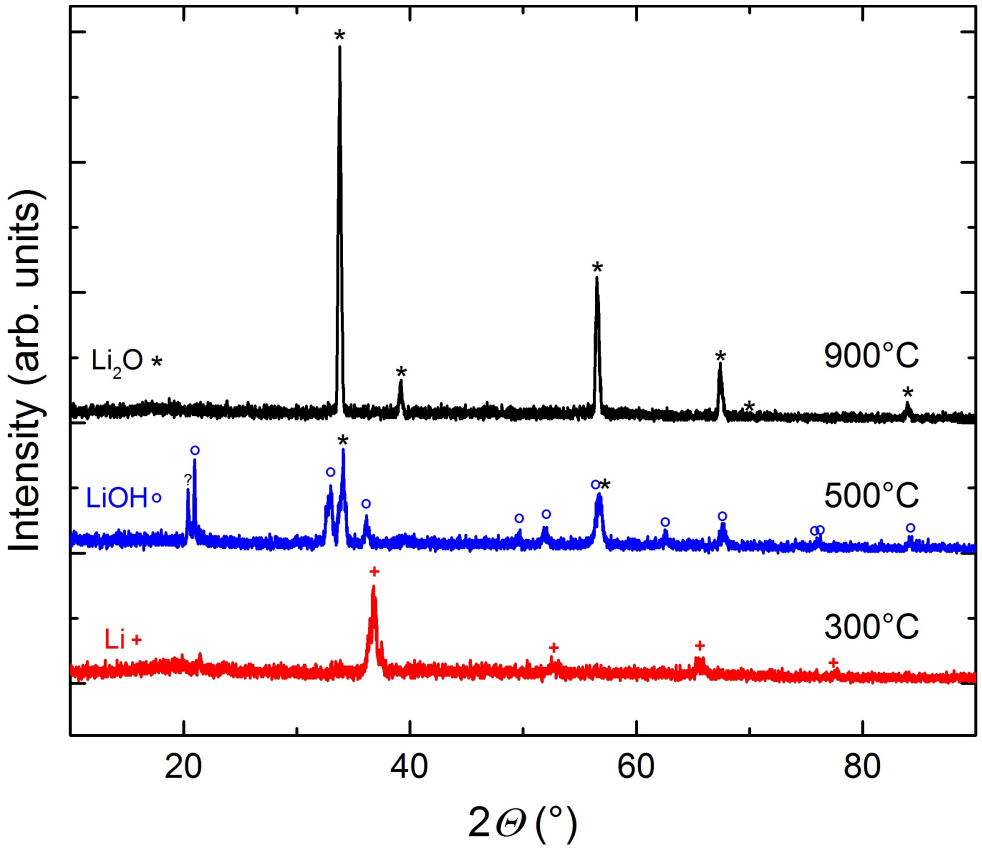

Supplementary Figure 2: Evolution of the lithium educt during the heating process. Three pieces of elemental lithium are placed in three alumina crucibles, put in an open box furnace at 200 °C and heated to 900 °C in four hours. The samples are taken out of the furnace during heating at 300 °C, 500 °C and 900 °C, respectively. Powder X-ray diffraction patterns, collected immediately after taking out the sample, show the transformation of lithium to a Li_2O-LiOH mix, ending in pure Li_2O. The theoretical peak positions of Li, Li_2O and LiOH are indicated in the patterns.

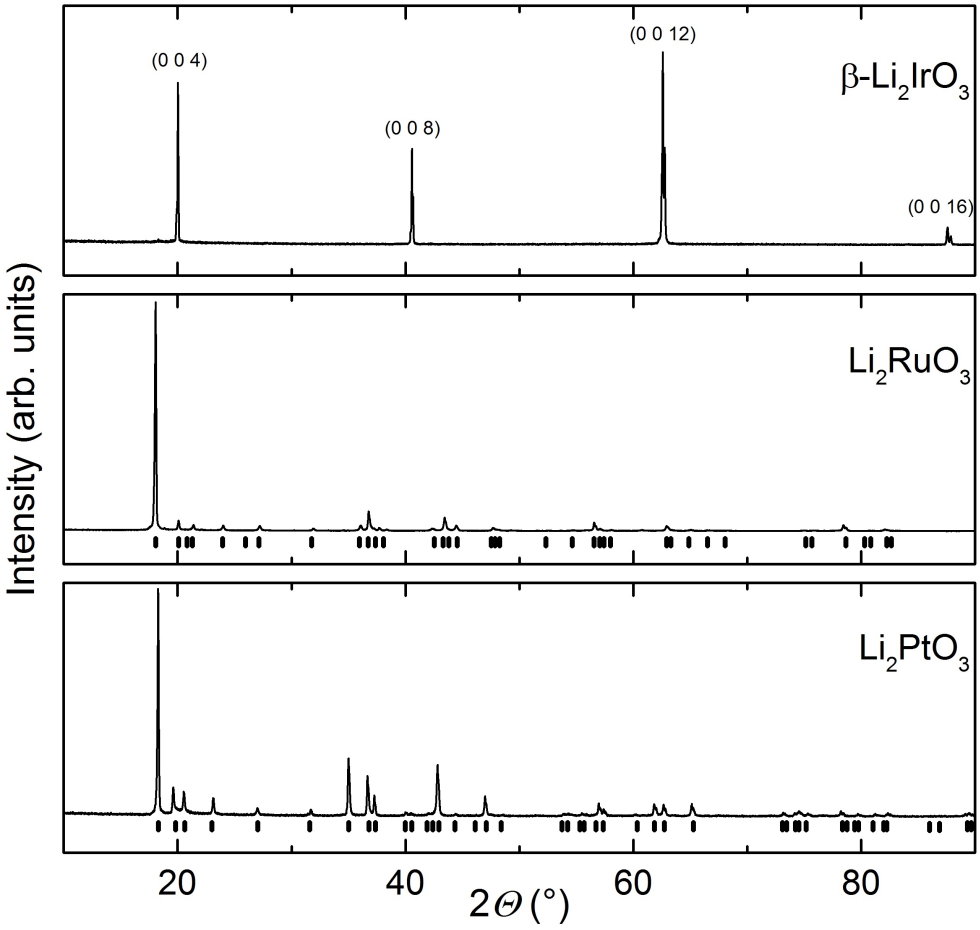

Supplementary Figure 3: X-ray diffraction patterns of β-Li_2IrO_3, Li_2PtO_3 and Li_2RuO_3 using a Rigaku powder diffractometer. A single crystal of β-Li_2IrO_3 was aligned with the (00l) plane satisfying the Bragg's law. For Li_2RuO_3 single crystals were crushed, while Li_2PtO_3 crystallized in well ordered powder. The samples are phase pure and all peaks can be indexed based on the reported crystal structures (black bars below the diffraction patterns). All samples are synthesized using separated educts (Li, Ir/Ru/Pt).

Supplementary Note

Crystal Structure of α-Li_2IrO_3

The crystal structure of α-Li_2IrO_3 is shown in Suppl. Fig. 4 and consists of an alternate stacking of honeycombs of edge-sharing IrO_6 octahedra with Li in the center, and hexagonal Li layers. Adjacent layers are stacked with an in-plane offset, leading to a monoclinic $C2/m$ space group [1]. Diffraction data were collected on 'Sample 1' (samples are described in the main text, alongside representative data, shown in Fig 4.a-b). The diffraction pattern could be fully indexed with a monoclinic unit cell with lattice parameters (Supplementary Table 2) consistent with earlier reports [1], with the empirical selection rules for the observed Bragg peaks $h + k =$ even, as expected for a C-centered cell in the ab plane. Importantly, this sample showed no observable diffuse scattering, which would constitute qualitative evidence for stacking faults, nor was there evidence for twinning (discussed below). This allowed for a single phase structural model to be considered without introduction of twin models or site-mixing approximations for disorder.

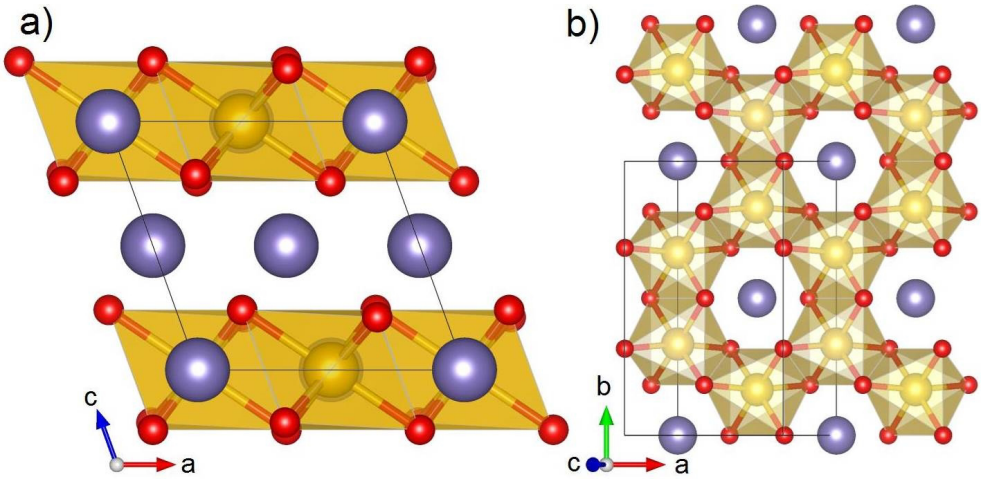

Supplementary Figure 4: Refined crystal structure of α-Li_2IrO_3, showing unit cell as a black outline, Ir as gold spheres, Li as purple and O as red. a) Projection onto the ac plane, showing the alternate stacking of $Li_{1/2}IrO_3$ and Li layers. b) Basal plane layer showing the honeycomb of edge-sharing IrO_6 octahedra.

We performed a full structural refinement of the crystal structure parameters against all integrated x-ray diffraction intensities. The refinement gave a good agreement between model and data as shown in Suppl. Fig. 5, with reliability factors $R(F^2) = 9.83\%$, $wR(F^2) = 14.6\%$, $R(F) = 5.82\%$ and $\chi^2 = 3.82$. The refined room temperature crystallographic parameters and quantitative details of the data collection are given in Supplementary Table 2, and the corresponding structure is drawn in Suppl. Fig. 4. In addition, we tested whether or not the crystal structure had lower symmetry than $C2/m$ by de-

scribing it within the corresponding $P\bar{1}$ primitive unit cell. This unit cell preserves all translational symmetry of the lattice, but only contains inversion symmetry. In this case, no improvement in the fit was achieved, and the same result was found within error as for the higher-symmetry, nominal $C2/m$ cell in Supplementary Table 2. Further tests to explore Ir disorder through site-mixing with the Li ions also showed no improvement in the refinement, leading us to the conclusion that Sample 1 has a fully ordered, layered iridium honeycomb lattice in all three dimensions. We note that a key difference between the solution presented herein and that published by O'Malley *et al.* is the z-coordinate of O2. In our solution, the oxygen ions lie more closely within a common ab-plane, as observed in Na_2IrO_3 [2].

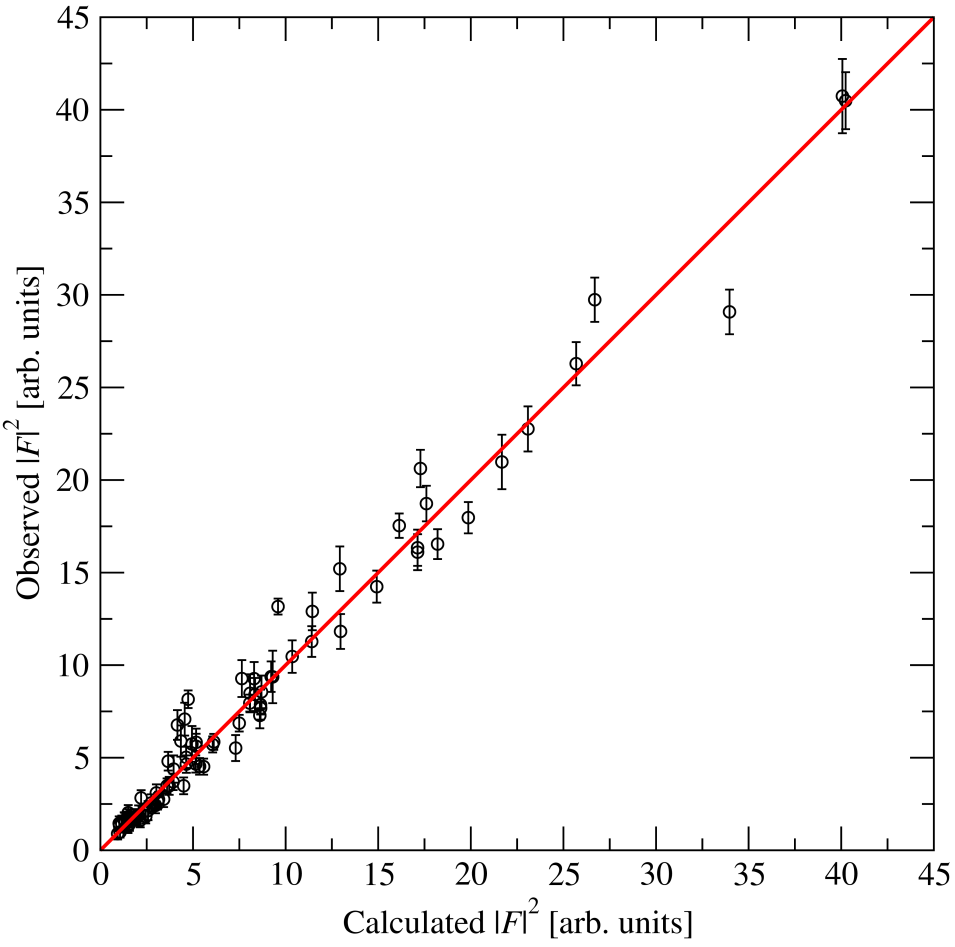

Supplementary Figure 5: Observed vs calculated $|F|^2$ values from Rietveld refinement of the $C2/m$ crystal structure against the single crystal diffraction data. The red line is a guide to the eye.

Supplementary Table 2: α-Li_2IrO_3 room temperature crystal structure. Standard errors on refined parameters are given in parenthesis. Note that lithium parameters were fixed to literature values [1].

Cell parameters

Space group: $C2/m$

Z = 4

a, b, c (Å)	5.1749(2)	8.9359(2)	5.1194(2)
α, β, γ (°)	90	109.827(5)	90

Volume: 222.70(2) Å^3

Atomic fractional coordinates

Atom	x	y	z	U_{iso}(Å^2)
Ir1	0	0.3331(4)	0	-
Li1	0	0	0	0.00633
Li2	0	0.809	0.5	0.00633
Li3	0	0.5	0.5	0.00633
O1	0.25(1)	0.321(5)	0.765(8)	0.03(1)
O2	0.27(2)	0	0.76(1)	0.03(1)

Ir anisotropic adps (Å^2)

U_{11}	0.019(7)
U_{22}	0.007(2)
U_{33}	0.028(3)
U_{12}	-
U_{13}	0.011(3)
U_{23}	-

Data collection

measured reflections: 2415

independent reflections: 83

Data reduction R_{int}: 5.76%

(Criterion for observed reflections: $I > 2.0\sigma(I)$)

observed reflections: 83

fitted parameters: 12

Stacking Faults in α-Li_2IrO_3

As discussed in detail in the case of the iso-structural Na_2IrO_3 [2], as a result of the near hexagonal symmetry of the honeycomb layers there is only a rather small energy cost associated with a honeycomb layer being displaced in-plane by $\pm\mathbf{b}/3$. The presence of such occasional in-plane displacements in the layer stacking sequence is manifested in the X-ray diffraction pattern by diffuse rods of scattering along the l direction with the selection rule $k = 3n + 1$ or $3n + 2$ (n integer) and $h + k =$ even (due to the C-centering). The diffraction patterns of two samples affected by stacking faults to different extents are compared in Fig. 4b−c in the main text and in the intensity profile in Fig. 4g in the main text. It is clear that while sample 1 shows very strong peaks at integer l with negligible diffuse signal in-between the sharp peaks, by contrast for sample 2 the Bragg peaks are very weak relative to the strong diffuse scattering, which extends across a wide range of l values.

Twinning in α-Li_2IrO_3

There is a high incidence of twinning in α-Li_2IrO_3 crystals. Most common are twins with the ab planes rotated relative to one another by 120° around the normal direction, $\mathbf{c}^*$. The occurrence of such twins can be understood as follows. In the nominal structure subsequent honeycomb layers are vertically stacked with an in-plane offset along the $-\mathbf{a}$ direction, see Supplementary Figure 4a. Since the honeycomb layers have a near three-fold rotational symmetry around the vertical axis, there would be only a small energy cost if the in-plane offset direction were to rotate in the ab plane by ±120°, and, if subsequent layers were then to stack according to this new offset direction, a new grain would form, rotated around the $\mathbf{c}^*$ direction of the primary grain. We label such a twin $C^{\pm}$, where the superscript indicates the sign of the ±120° rotation.

Another common twin (designated as type A) corresponds to a rotation by 180° around the (101) direction, which swaps the $\mathbf{a}$ and $\mathbf{c}$ axes. This might occur because the a and c lattice parameters are very similar in magnitude. A third type of twin found corresponds to a rotation by ±90° around the $(\bar{1}01)$ axis, designated as $B^{\pm}$. We note that for $a = c$ an A-type rotation is equivalent to two consecutive B-type rotations followed by a 180° rotation around (010), i.e. $A = 2_y(B^{\pm})^2$. For the given crystal structure the two-fold rotation around $\mathbf{b}$ leaves the atomic arrangement invariant as it is a symmetry operation of the $C2/m$ space group.

The above twinning types are summarized in Supplementary Table 3, where the last column gives the transformation matrix between the reciprocal space coordinates (h', k', l') of the rotated twin and the corresponding coordinates of the primary (un-rotated) twin, defined as

$$(hkl) = (h'k'l')\mathcal{M}. \tag{1}$$

For simplicity the transformation matrix is given in the case when the structure has a hexagonal metric, where $a : b : c = 1 : \sqrt{3} : 1$ and $\cos\beta = -1/3$ (the latter equation corresponds to eclipsed stacking at the third layer). Those conditions are satisfied in the actual crystal structure to better than 1.4%.

Fig. 4d in the main text shows the diffraction pattern for a multi-twinned crystal. Using

Supplementary Table 3: Common twinning types in α-Li_2IrO_3 crystals. Last column gives the transformation matrix $\mathcal{M}$ for the reciprocal space coordinates as defined in (1).

Type	Orientation	$\mathcal{M}$
A	rotation by 180° around (101), exchanges **a** and **c**.	$\begin{pmatrix} 0 & 0 & 1 \\ 0 & -1 & 0 \\ 1 & 0 & 0 \end{pmatrix}$
$B^{\pm}$	rotation by $\pm 90°$ around $(\bar{1}01)$, brings the $\pm\mathbf{b}^*$ axis along (101)	$\begin{pmatrix} 1/2 & \pm 3/2 & -1/2 \\ \mp 1/3 & 0 & \mp 1/3 \\ -1/2 & \pm 3/2 & 1/2 \end{pmatrix}$
$C^{\pm}$	rotation by $\pm 120°$around (001)	$\begin{pmatrix} -1/2 & \pm 3/2 & 1/2 \\ \mp 1/2 & -1/2 & \pm 1/6 \\ 0 & 0 & 1 \end{pmatrix}$

the transformation matrices for the various types of twins we identify the peaks near fractional positions $(0, 2, n + 1/3)$ (n integer) as being the nominal $(1\bar{1}n)$ reflections of a C^+ twin, whereas peaks near $(0, 2, n - 1/3)$ are the nominal $(\bar{1}\bar{1}n)$ reflections of a C^- twin. Similarly, the peaks near $(0, k, \pm 1)$, k = odd are identified as being the nominal $(\pm 1, -k, 0)$ reflections of an A twin. All peaks seen in the diffraction pattern can then be accounted for by an appropriate weighting of a primary grain with A, C^+ and C^- twins, compare Fig. 4d and h) in the main text. The presence of $B^{\pm}$ twins is most easily revealed by the diffraction pattern in the $(h0l)$ plane (not shown) via peaks at $(2n/3, 0, 2n/3)$ (n integer), which correspond to nominal $(0, \mp 2n, 0)$ reflections of the rotated grain. The B^+ or B^- twins can subsequently be distinguished for example by the diffraction pattern in the $(\bar{h}kh)$ plane (not shown) where the nominal (001) reflection of the twins will appear at $(-1/2, \pm 3/2, 1/2)$, respectively. We note that all the above types of twins could also occur in combination, i.e. an A type twin of the primary grain may have its own $C^{\pm}$ twins and so on.

References

[1] O'Malley, M. J., Verweij, H. & Woodward, P. M. Structure and properties of ordered Li_2IrO_3 and Li_2PtO_3. *J. Solid State Chem.* **181**, 1803 − 1809 (2008)

[2] Choi, S. K. *et al.* Spin waves and revised crystal structure of honeycomb iridate Na_2IrO_3. *Phys. Rev. Lett.* **108**, 127204 (2012).